

Research Article

Integration of Resonant Coil for Wireless Power Transfer and Implantable Antenna for Signal Transfer

Dong-Wook Seo, Jae-Ho Lee, and Hyungsoo Lee

Automotive IT Platform Research Section, Electronics and Telecommunications Research Institute (ETRI), 1 Techno Sunhwan-ro 10-gil, Yuga-myeon, Dalseong-gun, Daegu 42994, Republic of Korea

Correspondence should be addressed to Jae-Ho Lee; jhleel229@etri.re.kr

Received 12 April 2016; Accepted 26 May 2016

Academic Editor: Sanghoek Kim

Copyright © 2016 Dong-Wook Seo et al. This is an open access article distributed under the Creative Commons Attribution License, which permits unrestricted use, distribution, and reproduction in any medium, provided the original work is properly cited.

We propose the integration of the resonant coil for wireless power transfer (WPT) and the implantable antenna for physiological signal transfer. The integration allows for a compact biomedical implantable system such as electrocardiogram (ECG) recorder and pacemaker. While the resonant coils resonate at the frequency of 13.56 MHz for the WPT, the implantable antenna works in the medical implant communications service (MICS) band of 402–405 MHz for wireless communications. They share the narrow substrate area of a bar-type shape; the coil has the current path on the outer part of the substrate and the meandered planar inverted-F antenna (PIFA) occupies the inside of the coil. To verify the potentials of the proposed structure, a prototype is fabricated and tested *in vitro*. The power transfer efficiency (PTE) of about 20% is obtained at a distance of 15 mm and the antenna gain of roughly –40 dBi is achieved.

1. Introduction

Recently, with growing interests in U-healthcare, studies on the biomedical implant devices, such as capsule endoscope, pacemaker, electrocardiogram (ECG) recorder, neurostimulator, and retinal implant, have drawn high attention. For wireless communications with implanted units, the medical implant communication service (MICS) band (402–405 MHz) is recommended by the Federal Communications Commission (FCC). An implantable antenna works in human or animal body and ensures the wireless communications, and many researches on the implantable antenna design have also been carried out [1–9]. Unlike typical antennas used in the air, the implantable antenna should satisfy various requirements and constraints such as antenna shape, biocompatibility, miniaturization, and broad bandwidth. The shape and biocompatibility are mainly determined by the implant part of the body and a package material, respectively [10]. The well-known antenna minimization technique is to use the high-permittivity substrates (e.g., Rogers 3010/3210 with $\epsilon_r = 10.2$), which shorten the effective wavelength. In the structural aspect, the dipole with spiral arms [1], meandered planar inverted-F antenna (PIFA) [3], and spiral PIFA [4] has

been designed for this purpose. Additionally, the extended current path using slots or notches on the radiating patch [5] and the open-end slot antenna with a meandered slot on the top metal [6] are also suggested. Stacked structure is also introduced to reduce the antenna area, even if the pitch of antenna is higher [7–9].

On the other hand, the electric components of an implant device need a power source. Conventional biomedical implant devices have been supplied with electric power by an internal primary cell, which should be unfortunately replaced through a surgery with a discharge cycle. The wireless power transfer (WPT) has been considered a noticeable alternative [11] and has been studied to recharge an internal secondary cell. Recently, studies on the WPT have focused on transmitting not only several mW for small devices, but also several kW for electric vehicles. Moreover, various methods to improve the power transfer efficiency (PTE) have also been researched [12–14].

Early studies related to the implant device have used an inductive link to simultaneously implement wireless communication and wireless power transfer. In this case, the high Q-factor of resonant coils to achieve the high PTE brings about narrowing the communication bandwidth; the

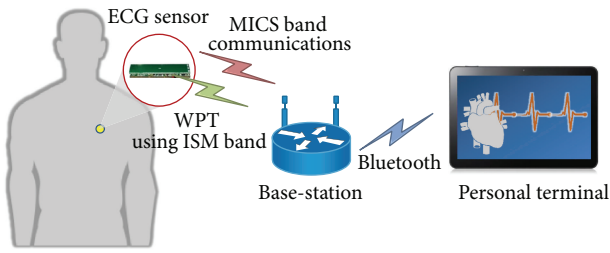


FIGURE 1: The concept developing the ECG monitoring system.

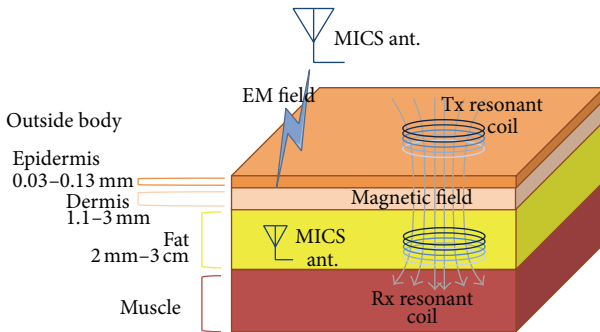


FIGURE 2: Inductive and electromagnetic links between the implant device and base-station.

tradeoff exists between the PTE and data rate. In order to overcome these disadvantages, the power allocation strategy using an orthogonal frequency-division multiplexing system is suggested [15]. However, in most recent researches, the WPT system operates at the industrial scientific medical (ISM) band, such as 6.78 MHz and 13.56 MHz, to easily implement a resonant coil with high Q-factor, and uses the outband communications to achieve the high data rate.

Our group has developed an ECG monitoring system as shown in Figure 1. An implant device communicates with a base-station using the MICS frequency band and transfers the sensed ECG signals to the exterior base-station. Consecutively, the collected ECG signals can be sent wirelessly to a personal terminal via Bluetooth. On the other hand, the power is wirelessly transferred from the base-station to the implant device at 13.56 MHz. That is, the base-station of the ECG monitoring system transfers simultaneously the power and signal into the implantable medical device using the outband communications.

Because the ECG signals are detected in the skin layer, the implant device is usually inserted in the subcutaneous fat layer for the ECG monitoring system as shown in Figure 2, and then the implant depth is about 3 mm to 20 mm. In our design concept, the implant device should have a bar-type shape in order to minimize the skin incision part, and the height of the implant board should be low to minimize the foreign body sensation of skin. In the MICS band, the transmit power has to be less than $25 \mu W$ (-16 dBm), and the MICS antenna should have the gain greater than

-45 dBi from the link budget analysis to achieve the minimum communication distance of 2 m. On the other hand, the gap between two electrodes of the ECG sensor should be larger than 30 mm in order to capture the stable ECG signal. Therefore, the implant coil size is set to $30 \text{ mm} \times 5 \text{ mm}$, while there is no size limit for the external coil. Since the power is transferred from the external coil to the implant coil only when the secondary battery needs charging, the external coil connected with the base-station is put on the skin or clothes only under charging. Therefore, the maximum distance between two coils is about 20 mm. In addition, because the implant device receives the signal and power source from the exterior base-station, the resonant coil and MICS antenna should be located on the outward surface of the implant device.

In [16], the Rx resonator operating at 6.78 MHz integrated with an antenna for the MICS band is proposed. Inserting the ferrite material below the coil generates the antenna current path. However, the height of integrated resonator and MICS antenna is not low due to the ferrite material.

In this study, integration of the coil and antenna on a common substrate is proposed for the implant device with low profile. Particularly, unlike most of the MICS antennas using substrate with high permittivity, the multilayer substrate of the ferrite sheet and FR-4 is utilized for significant size-reduction. Their potentials for the applications are verified by simulations and experiments.

In the following, we first present the proposed integration geometry of the resonant coil and MICS antenna. We then give details about design of integrated resonant coil with MICS antenna. And then, we describe the development of tissue-emulating materials that are used for *in vitro* measurements. Finally, we present simulation and measurement results.

2. Geometry of Resonant Coil and MICS Antenna

Figure 3 shows the configuration of the proposed integration of the Rx resonant coil and MICS antenna for the ECG monitoring system. The integration pattern module has a size of 225 mm^3 ($30 \text{ mm} \times 5 \text{ mm} \times 1.5 \text{ mm}$). A conducting meandered PIFA and upper coil pattern are printed on a 0.8 mm thick FR-4 substrate ($\epsilon_r = 4.4$, $\tan \delta = 0.013$) and the lower coil pattern is printed on the bottom of the FR-4 substrate. To isolate the implant device from the conductive tissue, the quartz superstrate ($\epsilon_r = 3.78$) packages the implant device. The ferrite sheet is inserted between the FR-4 and the ground plane to shorten the effective wavelength and shield magnetic field interfering with the other circuits.

As it can be observed from Figure 3(b), the prototype of the implant device consists of the bottom circuit module and top integration pattern module. The circuit module includes the MICS transceiver, ECG sensor part, impedance matching network, and charge circuit. The integration pattern module is the resonant coil integrated with the MICS antenna of Figure 3(a). The connection between the two modules is realized and fixed with a low-profile connector.

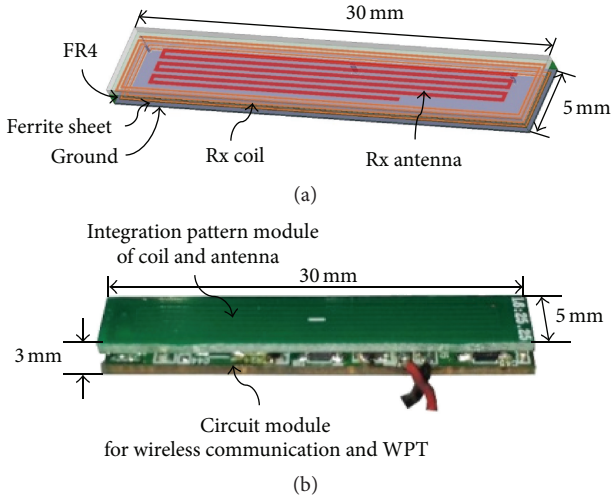


FIGURE 3: The proposed resonant coil and MICS antenna: (a) perspective view and (b) fabricated prototype of the implant device.

3. Integration of MICS Antenna with Resonant Coil

The integration pattern module has a narrow bar-type shape for easy injection with a guider such as the hypodermic syringe. The integration size is determined to be 30 mm \times 5 mm which is the same dimension as that of the bottom circuit module.

3.1. Design Process. Since the MICS antenna is located on the inner area of the Rx resonant coil, the MICS antenna and the resonant coil inevitably affect each other. Therefore, an integration design process is required in consideration of the mutual influence between the two elements, and it is illustrated on a flow chart shown in Figure 4. Once the implant depth is selected, system requirements can be translated into antenna requirements through a link budget analysis, and the coil size is determined by the maximum circuit board size and implant part of a human body. These requirements determine the materials for coil and antenna construction. In this study, the FR-4 and ferrite sheet are selected as substrates, and the quartz is selected as a superstrate. In the next step, the line width, the gap between the lines, and the number of turns and layers are designed. Coil parametric study and optimization are performed until the Q-factor is maximized in simulation.

A MICS antenna is first modeled, simulated, and optimized by finely adjusting the antenna size, gain, and matching point. In the next step, the unloaded Q-factor of the resonant coil is recalculated and is compared with the desired value. If the resonant coil fails to satisfy the desired Q-factor, the resonant coil and MICS antenna are redesigned until requirements are met. In the last step of the design process, the capacitance is calculated to make the resonant coil resonate at the operating frequency using the designed inductance.

3.2. Design of Rx Resonant Coil. The goal of coil design is to obtain the maximized unloaded Q-factor. It is widely known that the unloaded Q-factor of a coil has a tendency to

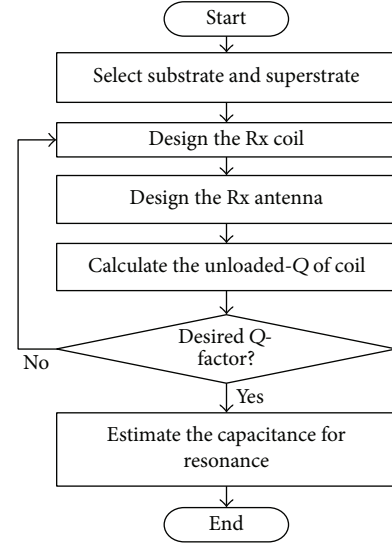


FIGURE 4: Design process of the integration of the resonant coil and MICS antenna.

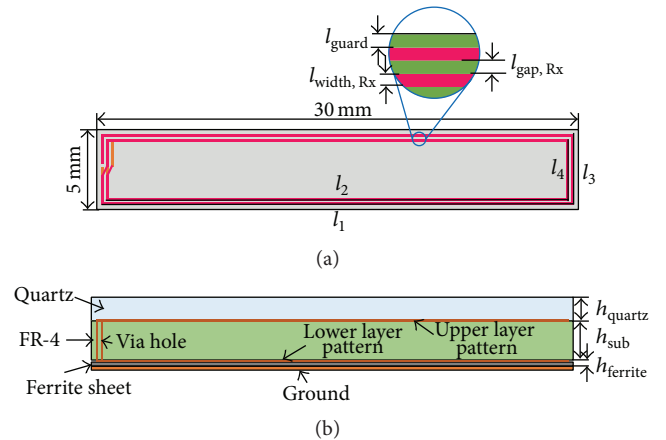


FIGURE 5: Geometry of the designed Rx resonant coil: (a) top and (b) side.

increase with the large inner area, wide line width, and long line length of the coil. However, if the line length exceeds a certain level, the ohmic loss becomes dominant rather than the inductance, and consequently the Q-factor of the coil decreases. Therefore, the design of Rx resonant coil will be completed after several iterations.

As shown in Figure 5, the Rx resonant coil has two-layer and four-turn structure. The coil patterns are printed on 0.8 mm thick (h_{sub}) FR-4 substrate, and 0.5 mm thick (h_{quartz}) quartz superstrate covers the structures to prevent it from directly contacting the lossy tissue. 0.2 mm thick ($h_{ferrite}$) ferrite sheet is used to reduce the ground effect and to prevent magnetic flux from interfering with the bottom circuit module.

It requires that the coil has the large inner area to secure an antenna region and to achieve the high Q-factor. Thus, the line width ($l_{width,Rx}$) and the gap ($l_{gap,Rx}$) between the lines have minimum values, 0.15 mm and 0.13 mm, respectively.

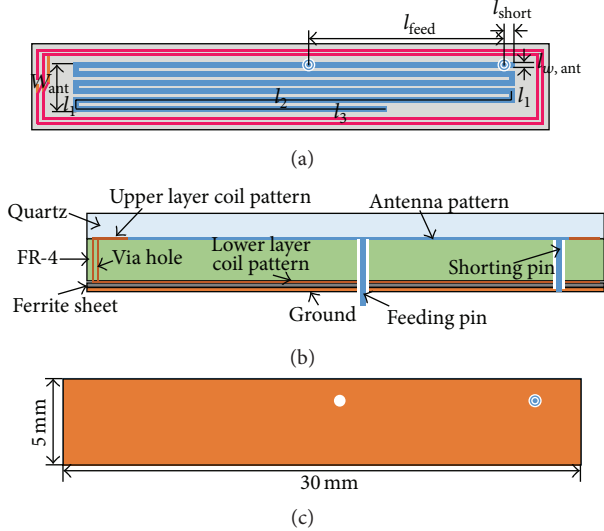


FIGURE 6: Geometry of the proposed resonant coil and MICS antenna: (a) top, (b) side, and (c) bottom.

The printed patterns are 0.3 mm (l_{guard}) apart from the edge of printed circuit board (PCB). The number of turns and layers is optimized using the high frequency structural simulator (HFSS) of Ansys.

3.3. Design of MICS Antenna. In our structure, the MICS antenna occupies the inner area of resonant coil, about 3 mm \times 28 mm. To reduce the antenna size, the meandered PIFA structure is adopted as shown in Figure 6. The resonant frequency is determined by the meandering path length and shorting pin position, and the antenna input impedance is controlled by the position of feeding pin. The antenna width (W_{ant}) is set to be 2.8 mm, and the line width ($l_{w,\text{ant}}$) is chosen to be 0.3 mm. The parameters (l_1 , l_2 , and l_3) related to the meandered line are finally determined to be 0.5 mm, 25.25 mm, and 17 mm for the antenna's resonance in the MICS band. The parameters (l_{feed} and l_{short}) relevant to the positions of feeding pin and shoring pin are 16.5 mm and 0.5 mm, respectively.

In comparison with usual substrates used for the implantable antenna, the FR-4 has relatively low permittivity, $\epsilon_r = 4.4$, while the ferrite sheet for shielding magnetic field by the coils has high permeability; its relative permeability is 131 at 13.56 MHz and 31 at 400 MHz. Therefore, the ferrite sheet with high permeability allows reducing the effective wavelength on the PCB. As a result, the meandered PIFA can be effectively minimized. Due to bottom ground plane, in addition, the antenna gain increases and the back lobe decreases.

4. Design of Tx Resonant Coil

Consider two coaxial circular coils with radii r_{Rx} and r_{Tx} , respectively. For the two paralleled coils separated by distance d , the mutual inductance is given by [17]

$$M = \mu_0 \sqrt{r_{\text{Rx}} r_{\text{Tx}}} \left[\left(\frac{2}{k} - k \right) K(k) - \frac{2}{k} E(k) \right], \quad (1)$$

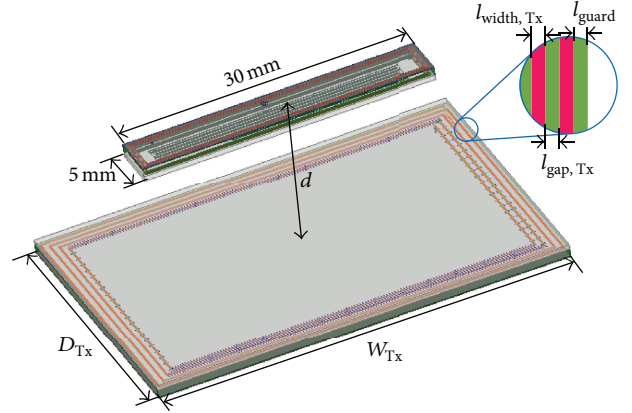


FIGURE 7: Geometry and comparison of the designed Tx coil and Rx coil.

where $K(k)$ and $E(k)$ are the complete elliptic integrals of the first and second kind, respectively, and

$$k^2 = \frac{4r_{\text{Rx}}r_{\text{Tx}}}{(r_{\text{Rx}} + r_{\text{Tx}})^2 + d^2}. \quad (2)$$

Maximum mutual inductance results in maximizing coupling coefficient in which the PTE becomes also maximized. Therefore, the maximum PTE can be achieved by using the condition of maximum mutual inductance in a given environment. Equation (1) is the monotonically increasing function of k . Assume that the radius of Rx coil is a constant a times the radius of Tx coil (i.e., $r_{\text{Rx}} = a \times r_{\text{Tx}}$); then we obtain the maximum value of k by differentiating (2), as follows:

$$\frac{\partial k}{\partial a} = 0 \implies r_{\text{Tx}} = \sqrt{r_{\text{Rx}}^2 + d^2}. \quad (3)$$

Therefore, the radius of the Tx coil size having maximum mutual inductance is determined when we know the radius of the Rx coil, r_{Rx} , and the distance between the coils, d .

In our case, the derived equation of (3) cannot be utilized straightforwardly due to the Rx coil of the bar-type shape, but it helps to establish a guideline of the Tx coil size. The distance between the coils is 15 mm, and the length from the center of Rx coil to its sides is set to r_{Rx} of (3). Therefore, the estimated length (D_{Tx}) and width (W_{Tx}) of Tx coil are 42.4 mm and 30.4 mm, respectively. The parameters of Tx coil are also optimized, and then the Tx coil has single layer and four turns, as shown in Figure 7. The line width ($l_{\text{width,Tx}}$) and the gap ($l_{\text{gap,Tx}}$) are 0.35 mm and 0.6 mm, respectively.

5. Simulation and Experiment

5.1. Fabrication of Tissue-Emulating Materials. To verify the potentials of the proposed structure, a prototype is tested *in vitro* using a tissue-emulating material, which is made of deionized water, saccharose, sodium chloride, agarose, and TX-150 (known as “super stuff”). The recipes of the tissue-emulating material equivalent to dry skin for 13.56 MHz and 402 MHz are presented in Table 1.

TABLE I: Recipe of human dry skin tissue-emulating material for 13.56 MHz and 400 MHz.

Freq. MHz	Agar/TX-150, w/w%	Sodium Chloride w/w%	Sacharose, w/w%	Aluminum powder, w/w%	H ₂ O, w/w%
13.56	9.8 (TX-150)	0.3	—	9.2	80.7
400	1.0 (Agar)	2.8	52.2	—	45.0



FIGURE 8: Measurement setup for tissue-emulating materials.

Figure 8 shows the measurement setup for tissue-emulating materials. We measured the permittivity in the range of 10 MHz to 500 MHz by using Agilent's E4991A impedance analyzer and Agilent's 85070E high temperature probe.

Figure 9 shows the measured relative permittivity and conductivity of the gel for 13.56 MHz and 402 MHz, the values of which are 282.5 and 0.24 S/m at 13.56 MHz and 43.2 and 0.704 S/m at 402 MHz. These measured values are within the error of 10% in comparison with the desired values ($\epsilon_r = 285.25$ and $\sigma = 0.238$ S/m at 13.56 MHz and $\epsilon_r = 46.7$ and $\sigma = 0.704$ S/m at 402 MHz for human skin).

5.2. Simulation and Experiment Results. The simulated and measured reflection coefficient frequency responses of the meandered PIFA antenna in the skin tissue model are presented in Figure 10(a). The measured frequency band is ranging from 325 MHz to 502 MHz with a -10 dB bandwidth criterion (from 350 MHz to 420 MHz in the simulation with the same criterion).

Figure 10(b) depicts the simulated gain radiation patterns in the xz - and yz -planes at 402 MHz. The maximum gain of -40.3 dBi is expected, whose value satisfies the antenna requirement as mentioned in Introduction.

At the resonant frequency of 13.56 MHz, the simulated and measured Rx coil parameters are presented in Table 2. Good agreement exists between the measured and simulated results. When the distance between the coils is 15 mm, the PTE is achieved about 20%.

6. Conclusion

In this paper, the integration of the resonant coil and MICS antenna with narrow bar-type shape is investigated. To design the compact integration module, the multilayer

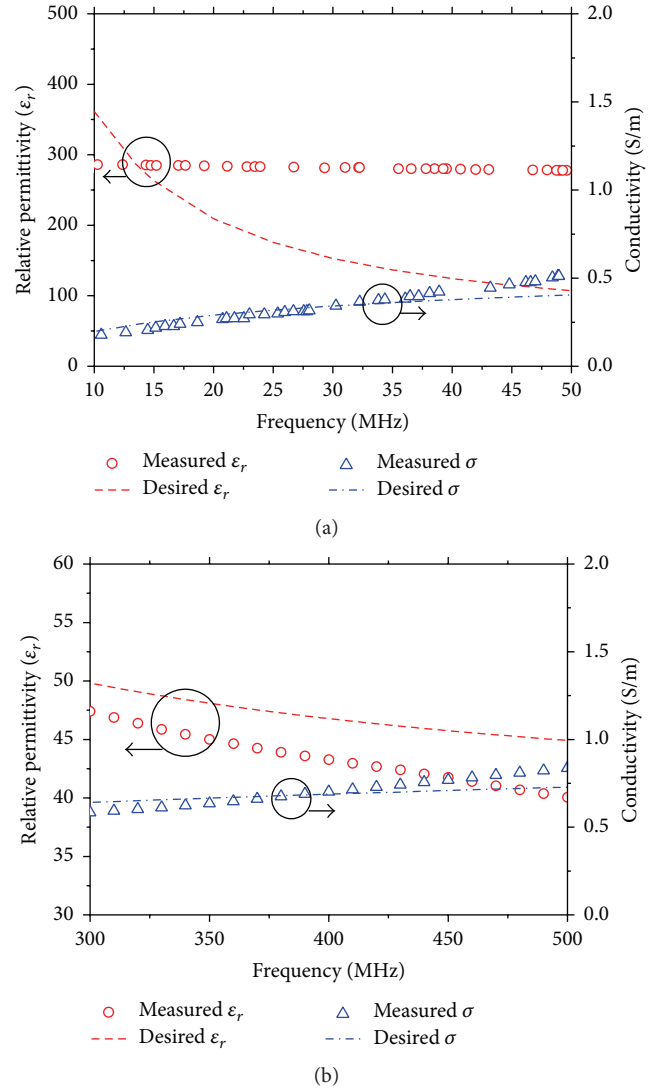


FIGURE 9: Measured permittivity and conductivity of the developed tissue-emulating materials: (a) for 13.56 MHz and (b) for 402 MHz.

TABLE 2: Rx coil parameters and power transfer efficiency.

Rx coil	Simulation	Experiment
L , nH	595.2	605.6
R , Ω	2.59	2.1
Q	19.6	24.57
k	0.034	0.035
η , %	19%	21%

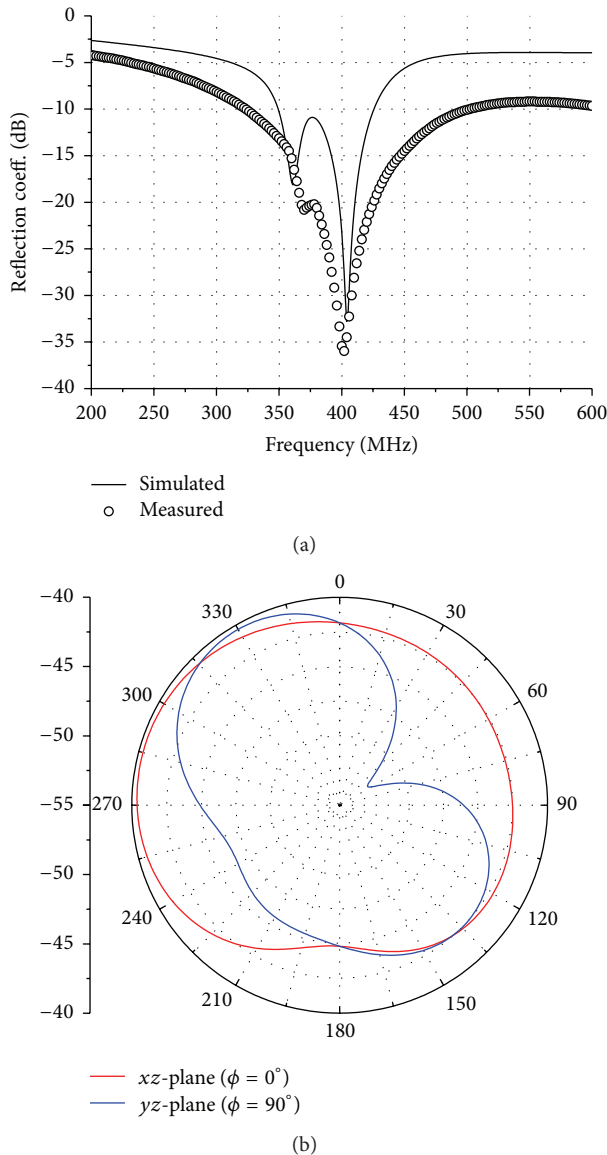


FIGURE 10: Performance of the designed MICS antenna: (a) simulated and measured reflection coefficient frequency response and (b) simulated far-field gain radiation patterns.

substrate of ferrite sheet and FR-4 is used instead of a high-permittivity substrate. On the common substrate, the resonant coil encloses the meandered PIFA. The proposed narrow bar-type structure can be suitable for the biomedical implant devices such as ECG recorder and pacemaker which are inserted into the subcutaneous tissue.

The potentials of the designed resonant coil and MICS antenna for implant device were completely demonstrated through fabrication of a prototype and measurement with tissue-emulating materials. In measurement, the MICS antenna had the frequency band ranging from 325 MHz to 502 MHz with a -10 dB bandwidth. The measured PTE between the designed Rx and Tx coils was 21% at a distance of 15 mm.

Competing Interests

The authors declare that they have no competing interests.

Acknowledgments

This work was supported by ETRI R&D Program [16ZC3300, Advanced Development of Fusion-Platform and Local Parts Maker Support Project for Context-Aware Smart Vehicle] funded by the Government of Korea.

References

- [1] J.-H. Lee, D.-W. Seo, and H. S. Lee, "Design of implantable rectangular spiral antenna for wireless biotelemetry in MICS band," *ETRI Journal*, vol. 37, no. 2, pp. 204–211, 2015.
- [2] A. Kiourti and K. S. Nikita, "A review of implantable patch antennas for biomedical telemetry: challenges and solutions," *IEEE Antennas and Propagation Magazine*, vol. 54, no. 3, pp. 210–228, 2012.
- [3] T. Karacolak, A. Z. Hood, and E. Topsakal, "Design of a dual-band implantable antenna and development of skin mimicking gels for continuous glucose monitoring," *IEEE Transactions on Microwave Theory and Techniques*, vol. 56, no. 4, pp. 1001–1008, 2008.
- [4] J. Kim and Y. Rahmat-Samii, "Implanted antennas inside a human body: simulations, designs, and characterizations," *IEEE Transactions on Microwave Theory and Techniques*, vol. 52, no. 8, pp. 1934–1943, 2004.
- [5] K. S. Nikita, J. C. Lin, D. I. Fotiadis, and M. T. Arredondo, "Editorial: Special issue on mobile and wireless technologies for healthcare delivery," *IEEE Transactions on Biomedical Engineering*, vol. 59, no. 12, pp. 3083–3089, 2012.
- [6] L.-J. Xu, Y.-X. Guo, and W. Wu, "Miniaturised slot antenna for biomedical applications," *Electronics Letters*, vol. 49, no. 17, pp. 1060–1061, 2013.
- [7] F.-J. Huang, C.-M. Lee, C.-L. Chang, L.-K. Chen, T.-C. Yo, and C.-H. Luo, "Rectenna application of miniaturized implantable antenna design for triple-band biotelemetry communication," *IEEE Transactions on Antennas and Propagation*, vol. 59, no. 7, pp. 2646–2653, 2011.
- [8] A. Kiourti and K. S. Nikita, "Accelerated design of optimized implantable antennas for medical telemetry," *IEEE Antennas and Wireless Propagation Letters*, vol. 11, pp. 1655–1658, 2012.
- [9] C.-M. Lee, T.-C. Yo, C.-H. Luo, C.-H. Tu, and Y.-Z. Juang, "Compact broadband stacked implantable antenna for biotelemetry with medical devices," *Electronics Letters*, vol. 43, no. 12, pp. 660–662, 2007.
- [10] K. Scholten and E. Meng, "Materials for microfabricated implantable devices: a review," *Lab on a Chip—Miniaturisation for Chemistry and Biology*, vol. 15, no. 22, pp. 4256–4272, 2015.
- [11] T. Sun, X. Xie, and Z. Wang, *Wireless Power Transfer for Medical Microsystems*, Springer, 2013.
- [12] D.-W. Seo, J.-H. Lee, and H.-S. Lee, "Optimal coupling to achieve maximum output power in a WPT system," *IEEE Transactions on Power Electronics*, vol. 31, no. 6, pp. 3994–3998, 2016.
- [13] D.-W. Seo, S.-T. Khang, S.-C. Chae, J.-W. Yu, G.-K. Lee, and W.-S. Lee, "Open-loop self-adaptive wireless power transfer system for medical implants," *Microwave and Optical Technology Letters*, vol. 58, no. 6, pp. 1271–1275, 2016.

- [14] D.-W. Seo, J.-H. Lee, and H. Lee, "Study on two-coil and four-coil wireless power transfer system using z-parameter approach," *ETRI Journal*, vol. 38, no. 3, pp. 568–578, 2016.
- [15] K. Lee and D.-H. Cho, "Simultaneous information and power transfer using magnetic resonance," *ETRI Journal*, vol. 36, no. 5, pp. 808–818, 2014.
- [16] A. Khripkov, W. Hong, and K. Pavlov, "Integrated resonant structure for simultaneous wireless power transfer and data telemetry," *IEEE Antennas and Wireless Propagation Letters*, vol. 11, pp. 1659–1662, 2012.
- [17] C. R. Paul, *Inductance: Loop and Partial*, John Wiley & Sons, New York, NY, USA, 2010.



Hindawi

Submit your manuscripts at
<http://www.hindawi.com>

